A Review of Dual Energy CT: Principles, Applications, and Future Outlook

Adam S. WANG[a,b✉], Scott S. HSIEH[a,b], Norbert J. PELC[a,b,c]

Departments of a) Electrical Engineering, b) Radiology, and
c) Bioengineering; Stanford University, Stanford, CA 94305

Abstract: The contrast properties of computed tomography (CT) depend significantly on the X-ray energy spectrum used to measure the object. Conventional CT uses only a single energy spectrum and at times suffers from ambiguity so that two different materials can appear identical. Dual energy CT (DECT) uses two different energy spectra that can be used to remove this ambiguity. Although the basic concept of DECT is not new, its popularity has recently skyrocketed because of the availability of commercial implementations. We review the basic principles of DECT physics and estimation, as well as the technologies that have enabled DECT to enter modern clinical imaging. Applications of DECT abound, and we familiarize the reader with a selection of the most common clinical applications. Finally, we conclude by touching on two areas of current technical development: photon-counting detectors and synthetic CT.

Key words: Dual Energy; Material Decomposition; Dual Source; Photon Counting; Synthetic CT

The goal of every medical imaging device is to produce an image of an underlying physical parameter of the scanned object. In computed tomography (CT), this physical parameter in question is the X-ray attenuation coefficient. Differences in the X-ray attenuation coefficient among tissues allows the anatomy to be non-invasively imaged, and can reveal abnormalities in the patient, which can then be used to make a diagnosis. The X-ray attenuation coefficient, however, is known to depend on the energy of the X-rays used to make the measurements. If imaging at a single energy produces an image of a single physical parameter, then it is only natural to suppose that imaging at multiple energies produces an image with multiple parameters, and that different materials could have their own distinct signatures in multi-energy CT imaging. For these reasons, the potential of imaging at multiple energies in CT was not lost on its inventors and comments pertaining to its use can be found as far back as 1973 by Hounsfield[1]. Indeed, multiple-energy imaging was sometimes called "tomochemistry" initially because of its potential ability to distinctly identify chemicals in its cross-sectional images.

Within three years, the basic principles of dual-energy imaging were understood, and it was soon appreciated that multiple-energy imaging directly measures only two physical quantities, which are the effective atomic number and the electron density[2-3]. These theoretical concepts were quickly tested on phantoms and in tissue[4-5], but early experiments were plagued by several

practical difficulties, including image mis-registration, imperfect beam hardening corrections, and poor stability. Initial implementations of DECT were poor. A dual crystal implementation of dual energy, which is an analog of the modern dual layer detector implementation, was presented early on and its poor spectral separation was realized[6]. A prototype of the modern rapid kVp switching scanner was likewise presented very early on[7]. Other implementations were proposed in this period, including a split-filter design to separate the fan-beam into high and low energy components[8], and an alternating filtration pattern on the detector[9]. All of these implementations suffered drawbacks and none of them had long term clinical adoption.

The major reconstruction concepts and several potential applications were seen early on. A decade after the introduction of CT, our understanding of DECT was remarkably complete. Advances were made along both projection-space reconstruction methods[10-11] and image-space reconstruction methods[12]. The most popular application was in the measurement of bone density in the vertebrae, which could have been useful in the diagnosis of osteoporosis. Because of its ability to distinguish between materials, dual energy imaging was appreciated as being potentially more accurate than single energy imaging for determining bone mineral content[13-16]. Other applications included the measurement of iron in the liver[17] and the detection of calcium in lung nodules[18]. Despite the strength of this early work, DECT languished for decades. Practical difficulties continued to undermine adoption and were solved only with modern implementations of DECT.

The underlying physics of dual energy CT (DECT) is now well studied and understood. While imaging at a single energy gives us information of the X-ray attenuation coefficient at one energy, in most circumstances imaging at multiple energies provides redundant information on only two physical quantities, which are generally referred to as the density of the two *basis materials*. The nature of these basis materials lies at the heart of DECT, and they can often be chosen so that they have physical and clinical significance. For example, iodine can be chosen to be a basis material, and an image of the distribution of iodinated contrast media would have significant utility in a perfusion or angiography study. We will begin this review article by discussing the physics of DECT in greater depth, along with the mathematical algorithms used to estimate the basis materials from the dual energy measurements. We will also discuss the recent commercial implementations of DECT that have served to popularize the technique in recent years, along with some of their strengths and drawbacks. The availability of DECT has been followed by a host of clinical applications of the technique. It is beyond the scope of this work to provide details on all the uses of DECT, but we provide a sampling of some of the most common uses to give the reader an understanding of how DECT may be used in clinical practice. We also discuss some of the upcoming technical developments, including photon-counting detectors and synthetic CT.

1 Principles

The underlying principles of DECT are best understood by first examining the physical mechanisms of X-ray contrast.

1.1 Physics

The fundamental contrast mechanism for CT is the ability of tissue to scatter or absorb X-ray photons. The behavior of this attenuation is governed by the Beer-Lambert Law. For $I_0(E)$ photons

incident on a homogeneous object of thickness t and linear attenuation $\mu(E)$, the Beer-Lambert law states that the number of transmitted photons $I(E)$ can be expressed as

$$I(E) = I_0(E)e^{-\mu(E)t} \tag{1}$$

The X-rays employed in medical imaging generally have energies that range from 10 to 150 keV. In this diagnostic energy range, the interactions between matter and X-rays predominantly arise from two mechanisms: photoelectric absorption and Compton scattering[19]. In photoelectric absorption, the X-ray photon transfers all its energy to an atom, ionizing an electron, and disappears. In Compton scattering, the X-ray photon loses some of its energy to an electron, and propagates in a different direction, conserving energy and momentum. A third mechanism, Rayleigh scattering, will be ignored since it plays little role in diagnostic imaging. For an X-ray photon with energy E, the total amount of attenuation per unit length of matter is characterized by the linear attenuation coefficient $\mu(E)$, which leads to exponential attenuation.

The two physical mechanisms for attenuation, photoelectric absorption and Compton scattering, depend not only on the X-ray energy but also on the object. The object-dependent parameters are the effective atomic number Z_{eff} and the electron density ρ_e. These two properties are the driving force behind the difference in attenuation between two different materials such as bone and tissue. In fact, the probability of Compton scattering is proportional to the electron density (which, with the exception of hydrogen, is roughly proportional to the mass density) and photoelectric absorption increases with higher Z_{eff} and mass density ρ. Therefore, calcium ($Z = 20$) will be more attenuating than aluminum ($Z = 13$) at the same mass density. In particular, the attenuation $\mu(E)$ is the sum of the photoelectric $\mu_P(E)$ and Compton $\mu_C(E)$ components, which can be approximated by

$$\mu_P(E) = \rho_e \, C_P \, \frac{Z_{\text{eff}}^{3.8}}{E^{3.2}} \tag{2}$$

$$\mu_C(E) = \rho_e \, f_{KN}(E) \tag{3}$$

where C_P is a constant and the Klein-Nishina function $f_{KN}(E)$ is a decreasing function of E[19]. Note that both $\mu_P(E)$ and $\mu_C(E)$ are decreasing functions of E, so that higher energy X-rays are less attenuated. The photoelectric absorption, which is dominant at low energies, quickly decreases, while the Compton attenuation falls off much slower and is important at higher energies (Fig. 1(a)). The photoelectric absorption (Eq. 2) expression does not account for K-edges, which will be discussed later.

Let us call $E^{-3.2}$ and $f_{KN}(E)$ the photoelectric and Compton basis functions, respectively. Then any material's attenuation as a function of energy is a linear combination of these basis functions, where the weight of each basis function depends on the electron density ρ_e and effective atomic number Z_{eff}. Given the above equations, it should be clear that if an object's attenuation can be measured with at least two different energies, then the object-specific parameters ρ_e and Z_{eff} can be determined by *decomposing* the material's attenuation into the amount of each physical basis function. For example, if the object is measured with two different monoenergetic beams, the above equations will give us a system of equations from which ρ_e and Z_{eff} can be easily found. These two parameters can be very useful in identifying an object's composition, as first reported in the seminal paper by Alvarez and Macovski[2].

(a) Mass attenuation of Al   (b) Mass attenuation of H2O, Ca, I
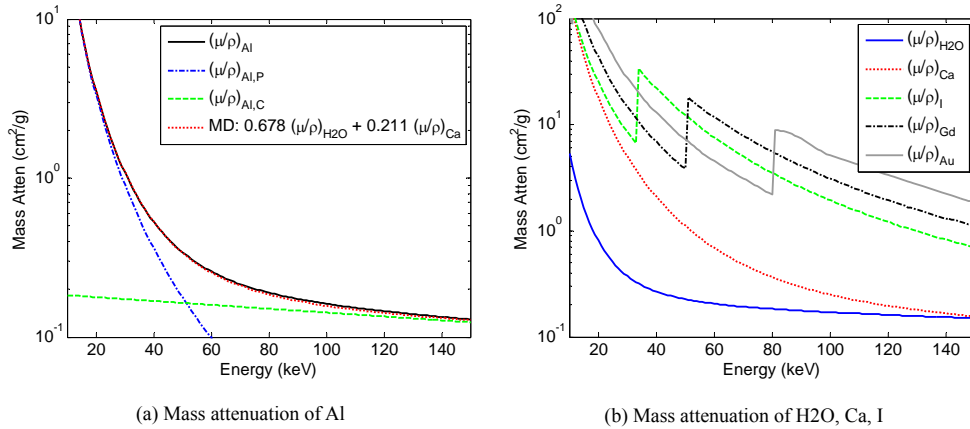
Fig.1   The mass attenuation of several materials are plotted as a function of energy. The
contributions from photoelectric absorption and Compton scatter are shown for aluminum,
as well as the material decomposition into water and calcium. Note the prominent K-edge at
33.2 keV for iodine, as well as the K-edges for gadolinium and gold, which increase in
energy with increasing atomic number

In addition to representing a material as a linear combination of the physical basis functions
(photoelectric absorption and Compton scattering), any material can be represented as a linear
combination of two other (different) materials since these other materials are themselves a linear
combination of the physical basis functions. To be concrete, the attenuation of water can be
written as a linear combination of the photoelectric and Compton basis functions. Calcium, too,
can be written as a linear combination of the photoelectric and Compton basis function.
Aluminum could also be written as a linear combination of the photoelectric and Compton basis
functions, but it could be equally well described as being a linear combination of water and
calcium simply by solving a system of linear equations. In fact, in terms of the mass attenuation,
which is the linear attenuation divided by the mass density, we have that

$$\left(\frac{\mu}{\rho}\right)_{Al}(E) = a_1\left(\frac{\mu}{\rho}\right)_{H_2O}(E) + a_2\left(\frac{\mu}{\rho}\right)_{Ca}(E) \qquad (4)$$

where $a_1 = 0.678$ and $a_2 = 0.211$. In other words, an area density of 1 g/cm^2 of Al is indiscernible
from an area density mixture of 0.678 g/cm^2 water and 0.211 g/cm^2 calcium by X-rays of any
energy. This illustrates that the attenuation of an unknown material can be decomposed into
two basis materials (such as water and calcium). This decomposition can be performed as
long as the two materials are not degenerate, or in other words, as long as Z_{eff} of the two basis
materials are not the same. Although nearly any two basis materials will work, it is often
useful to choose basis materials that have physical interpretations. For example, when
imaging the human body water and calcium may be a good choice – soft tissue will be
decomposed mostly into water since its Z_{eff} is close to water, while bone will have a
substantial calcium component. One limitation of dual energy is that some ambiguity still
remains. The aluminum previously described remains indiscernible from the mixture of water
and calcium that it can be decomposed into. A hypothetical extension to "triple energy"
imaging would not be helpful in this regard since the attenuation of all these materials are
fundamentally well described by only two basis functions. Therefore, basis materials should

be carefully chosen so that they are suitable for the imaging task.

The vast majority of the human body is composed of atomic elements of $Z \leq 30$. However, a contrast agent may be introduced that increases the local attenuation. For example, if iodine is introduced into the vasculature, it increases the attenuation wherever it travels to, in large part due to the high atomic number of iodine ($Z = 53$). Besides simply increasing the effective atomic number Z_{eff}, however, the attenuation function of iodine also features a large and sudden increase at 33.2 keV, known as the K-edge (Fig. 1(b)). The K-edge energy is the binding energy of a K-shell (innermost) electron. Only photons exceeding this energy can eject these K-shell electrons, as indicated by the discontinuity in attenuation at the K-edge. Iodine will much more strongly attenuate photons with energies just exceeding 33.2 keV than photons just under 33.2 keV. The K-edge energy increases with atomic number Z – for instance, the K-edge of Gd ($Z = 64$) is 50.2 keV and Au ($Z = 79$) is 80.7 keV.

For elements with $Z \leq 30$, the K-edge energy lies well below the diagnostic energy range and can therefore be neglected. Clearly, the K-edge introduces a new basis function since the attenuation curve cannot be represented by the continuous Compton and photoelectric basis functions alone. However, for diagnostic imaging, the vast majority of the transmitted X-rays have an energy greater than the K-edge of iodine since their average energy is well above 33 keV and photons with energy less than 33 keV do not penetrate the body easily. In this case, for energies above the K-edge, the attenuation of iodine *can* be modeled by the Compton and photoelectric basis functions. Therefore, to utilize iodine's K-edge, the incident X-ray spectrum must contain a significant number of photons with energy less than 33 keV and the object needs to be sufficiently thin, such as in preclinical or breast imaging.

1.2　Implementation

As the name "dual energy" suggests, it is necessary to image with X-rays of two different effective energies. Viable implementations of dual energy CT must satisfy two requirements. First, the effective energies of the spectra should have a sufficiently large separation so that the difference in attenuation between the energies is significant. When the energy separation is small, the noise of the material decomposition becomes large and the images become unusable. Second, the time between the two acquisitions at different energies must be short. For stationary objects, dual energy imaging could be implemented simply by taking two sequential scans at different energies, but in applications with living organisms the errors resulting from motion or contrast uptake/washout would become excessive. The recent, widespread adoption of dual energy into clinical CT scanners is largely due to implementations of DECT that satisfy both these requirements, as well as the other capabilities of modern CT scanners, such as high temporal and spatial resolution. There are four primary system strategies used for dual energy imaging: dual source, rapid kVp switching, dual layer detectors, and energy-resolving photon counting detectors. We will describe the first three here, and discuss photon counting later.

Both dual source and rapid kVp switching utilize measurements with two different peak X-ray tube voltages (kVp), and are both therefore dual kVp approaches. The low and high kVp beams have different effective energies, where tube limits provide an upper bound to the tube voltage and the need for photons with intensity and energy high enough that the object can be penetrated place a lower limit on kVp. A dual source system utilizes two source-detector pairs in the gantry (Fig.2). One source is operated at a lower voltage (e.g., 80 kVp), while the other source is operated at a higher voltage (e.g., 140 kVp). Because the source-detector pairs are

approximately in orthogonal directions, they can be operated simultaneously. After one rotation, a complete CT data set is acquired at both the low and high energies. Because both tubes are operated independently, it is easy to use different filtrations, and a beam hardening filter such as tin on the high energy can greatly increase the energy separation between the two spectra[20-21]. However, there are drawbacks to the system design including the increase in hardware cost and complexity due to the extra source-detector pair. Motion during the acquisition can result in collected data that is not perfectly registered between the low and high energy scans. Finally, cross-scatter from one source to the other detector can be a challenge when the sources are operated simultaneously[22].

Another approach to dual kVp is to use a single source that rapidly switches between tube voltages (Fig.3). While it is possible to scan once at low energy followed by another scan at high energy (or vice-versa), this so-called slow kVp switching suffers greatly from patient motion or different contrast distributions between the scans. Therefore, rapid kVp switching is used, whereby the source alternates very rapidly between low and high kVp as the source-detector pair rotates about the object. The difference in time between successive low and high energy projections is very small, providing well-registered and motion free projection pairs. The switching frequency is high enough that a sufficient number of projections equally spaced in angle are acquired with each spectrum.
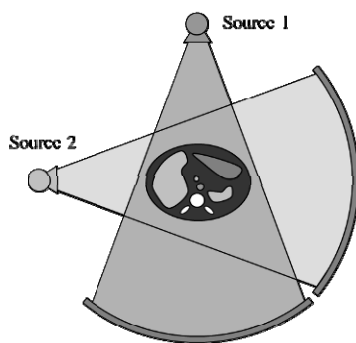

Fig.2. Dual source geometry. Two source-detector pairs operate simultaneously as they rotate around the patient. In DECT mode, one source is operated at a lower kVp than the other (e.g., 80 and 140 kVp)
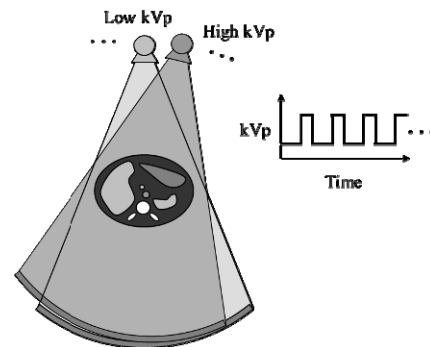
Fig.3 Rapid kVp switching geometry. The tube voltage rapidly oscillates between the low and high kVp as the source rotates about the patient, and these interleaved projections are captured separately by the detector

There are a number of technical challenges with this approach, most notably the kHz-rate changing of X-ray tube voltage from 80 to 140 kVp. Ideally, the voltage would change instantaneously, but in practice it will have some finite voltage slew rate that may reduce the spectral separation[23]. Changing the tube current in synchrony with the rapid kVp switching is also very difficult, so differences in mAs between the low and high energy projections can be accomplished with control of the dwell time at each voltage. Finally, although in principle a synchronized switching filter can be used to provide different filtration to each spectrum, mechanical constraints may preclude this and it is not currently implemented[24]. It is important to note that in each of these dual kVp techniques, the dose is not necessarily increased; instead it is split between the two energies and can still provide additional information for comparable dose to

a single kVp acquisition[25-26].

The other class of systems used for dual energy systems are energy-sensitive detectors, including dual layer and photon counting detectors, which generally utilize a single kVp spectrum. A dual layer, or sandwich, detector is comprised of a thin top scintillator that is more sensitive to low energy photons and a bottom scintillator that absorbs the remaining photons (Fig.4)[27-28]. Because the top scintillator's attenuation is greater at lower energies than at higher energies, it selectively absorbs more low energy photons, while high energy photons are more likely to penetrate the top layer and be absorbed in the bottom layer. The effective spectrum for each layer is also shown in Fig. 4. It has the advantage of perfect spatial registration between the low and high energy projections, but suffers from poor energy separation, even with selection of optimal thicknesses for the top layer, bottom layer, and filter in between[29].
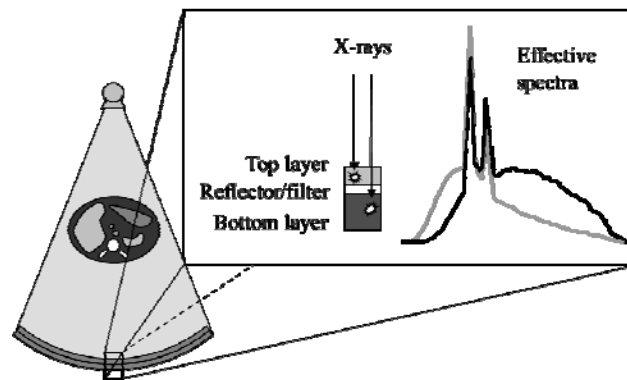
Fig.4   Dual layer geometry. The X-ray tube is operated at a single kVp, and energy specific information is captured by the layered detector. The effective spectrum for each layer demonstrates that the top layer is more sensitive to lower energies, while the bottom layer captures more of the higher energies

1.3   Estimation

The material decomposition estimation problem can be viewed simply as: given two measurements, solve for two unknowns. The two measurements come from the dual energy data, while the two unknowns are the material specific decompositions. There are two domains in which the estimation can be done: image space or projection space. In the image space approach, the dual energy scans are first reconstructed to form low and high energy images. These images are then used to estimate material specific images. In projection space, each line integral is decomposed into a line integral through each basis material. The resulting material sinograms can then be reconstructed to form the basis material images.

Image space decomposition is especially suited for unregistered data or if there is motion. The dual energy data could be acquired from two entirely different trajectories, but if the same location of the object is reconstructed, the images can be paired together. Consider a cylindrical acrylic (PMMA) phantom filled with solutions of different iodine concentrations scanned at 80 kVp and separately at 140 kVp (Fig.5). Due to the different effective energies of the spectra, the iodine contrast is markedly different. A weighted combination of the images can recover the iodine image or (with different weights) the water image. However, this is the case only if the two

images are equivalent to monoenergetic images; otherwise, the material decomposition will be imperfect due to beam hardening. Nonetheless, linear (or even nonlinear) combinations of the images, known as mixed images, can be formed in such a way that the contrast-to-noise ratio (CNR) is maximized for a particular imaging task[25,30], or so that a material (like iodine) is fully canceled. Moreover, the dual-energy index (DEI) can be calculated and is useful for material identification, where x_{low} and x_{high} are the voxel values (in Hounsfield units) of the low and high energy images[31].

80 kVp Image   140 kVp Image

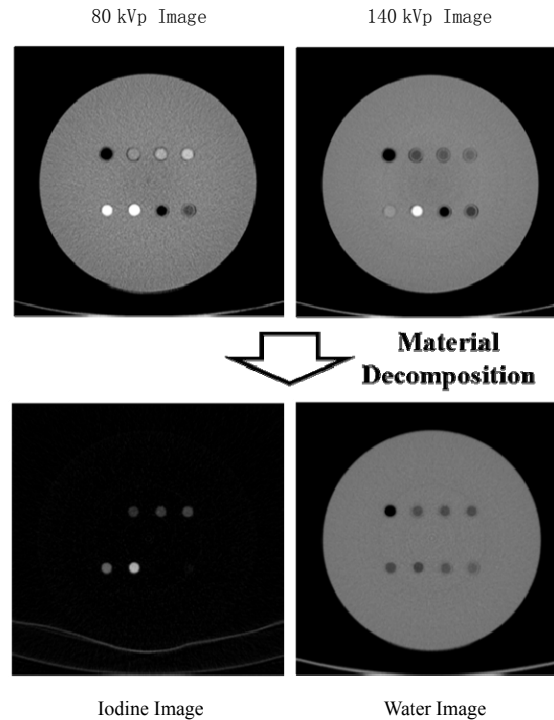Iodine Image   Water Image

Fig.5 Image space decomposition. The 80 and 140 kVp images of this phantom are used to form an iodine and water image. The iodine is clearly separated from the rest of the object and quantitatively matches the iodine concentration of the solutions. Note that the patient table appears in both images since it is neither water nor iodine

$$DEI = \frac{x_{low} - x_{high}}{x_{low} + x_{high} + 2\,000} \tag{5}$$

Alternatively, material decomposition can be done in projection space by decomposing each line integral into line integrals of the basis materials. The resulting basis material sinograms can then be reconstructed to form basis material images (Fig.6). Algorithms for estimating the decomposition include maximum-likelihood estimation (MLE), linearized (weighted) least squares, or a polynomial fit to calibration data. In particular, MLE attempts to solve the question: given low and high energy measurements $d = (d_l, d_h)$, what decomposition $t = (t_1, t_2)$ is the most likely to have produced those measurements? Mathematically, the estimated decomposition $\hat{t}$

can be described as

$$\hat{t} = \arg\max_{t} f(d \mid t) \qquad (6)$$

where $f(d \mid t)$ is the probability density function of measurement d from an object with decomposition line integral t. Because MLE models the physical and statistical processes of how the data was acquired, it is also well suited for the over determined case when more than two energy-sensitive measurements are acquired[32-34]. A linearized weighted least squares approach can also handle the over determined case well by weighting each measurement depending on its statistics[35]. The polynomial fit uses calibration data to fit a polynomial function that maps measured data to the material thickness[36]. Both the linearized weighted least squares and a polynomial fit can be computed quickly, while MLE requires solving an optimization problem.
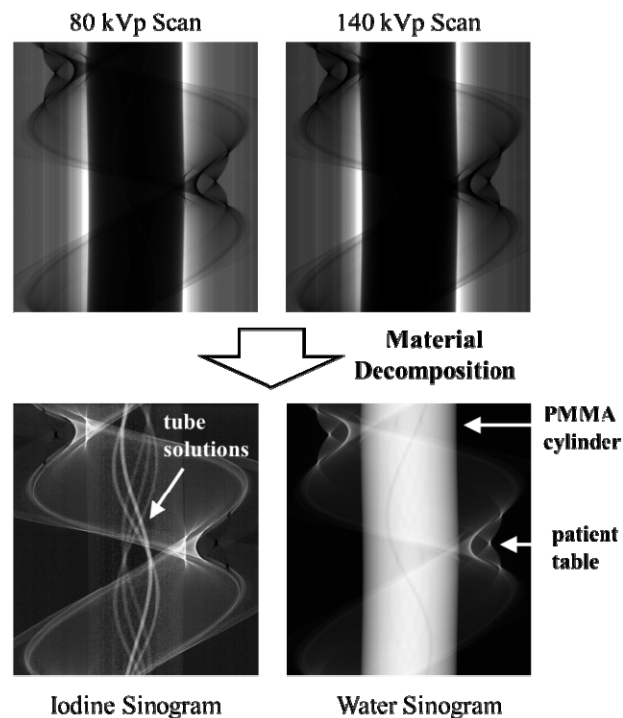

Fig. 6   Projection space decomposition. The raw data, shown as a sinogram, is used to estimate the line integrals of iodine and water. These material decomposition sinograms can then be reconstructed separately

Projection-based methods have the key advantage of inherently handling beam hardening, caused by the preferential attenuation of the lower energies in polyenergetic spectra (Fig.7). However, this technique generally requires the data to be well registered or else the errors will be quite large-different low and high energy trajectories make projection space decomposition impossible, as do motion or data inconsistencies.

In both image- and projection-based methods, noise in the dual energy measurements leads to noise in the material decomposition. For measurements with uncorrelated noise (commonly the case), the decomposition noise is negatively correlated. When performing dual energy

decomposition from two measurements, the noise is usually the same in all methods, but when using three or more measurements to calculate two unknowns (an overdetermined problem), the estimation needs to be done carefully to minimize the estimation noise by accounting for the statistics in each measurement.
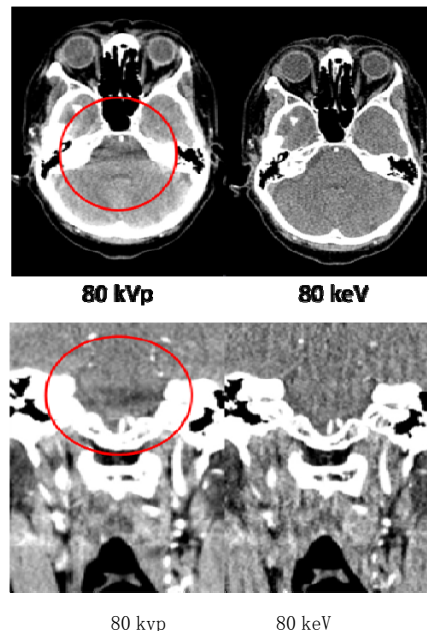

Fig. 7   Axial and coronal reformat images of the brain. Note the severe beam hardening artifact between the bones in the 80 kVp (polyenergetic) images. These artifacts are no longer present in the 80 keV (monoenergetic) images due to the projection-based material decomposition used to form the monoenergetic image. Images courtesy of Dr. Amy Hara, Mayo Clinic, Scottsdale, AZ

The material decompositions can be combined to meet task-specific objectives, such as forming the highest iodine CNR image. In particular, a weighted sum of the images, where the weights are the attenuation of each basis material at energy E, yields a monoenergetic image of energy E. It is an estimate of the image that would have been produced if the object was scanned with a monoenergetic beam of that energy. Generally, monoenergetic images in the range of 60-75 keV have the lowest noise as they combine the material decompositions such that the negatively correlated noise tends to cancel. The material-specific images are themselves useful -- for example, the iodine image can be color overlayed on a grayscale anatomic image so that the distribution of iodine can be visualized. Furthermore, for a water/iodine decomposition, the water image is inherently free of iodine and is used as a virtual non-contrast (unenhanced) image. Finally, in addition to the simple image- and projection-based methods, we note that DECT lends itself well to iterative reconstruction techniques since all attenuation processes can now be modeled and measured[37].

3   Current Applications

Dual energy has previously been used in radiography (e.g., chest), dual energy X-ray absorptiometry (DEXA), security applications, and non-destructive evaluation. When used for

chest X-rays, for example, an image can be formed that effectively removes the skeleton to form a soft tissue image where the bones are not obstructing the view of potential pathology in the lungs or heart[38]. Conversely, a bone image can be formed to examine the skeleton and calcified lesions. DEXA uses dual energy measurements to quantitate areal bone mineral density for osteoporosis risk assessment[39-40]. Baggage scanners in airports commonly utilize dual energy X-ray radiography and/or CT to screen for explosives and contraband[41-43]. Finally, the application of DECT to non-destructive evaluation is as far reaching as imaging nuclear waste drums[44], gas-solid flows in process engineering[45], and geologic samples of rocks or soil[46-47]. The many industrial applications of dual energy imaging follow many of the same principles and goals of clinical DECT, which we provide an overview of in the remainder of this section.

With the recent commercially available implementations of dual energy CT, many applications are being adopted or actively investigated for clinical practice. A recent book, edited by Johnson et al[48], thoroughly describes current clinical applications of DECT and is highly recommended for further reading. Most of DECT's applications can be traced back to its ability to do material specific imaging. Clinical images are often viewed with a certain material (e.g., iodine) presented as a color overlay on a grayscale CT anatomic image, or with a certain material (e.g., calcium) removed.

In fact, the ability to differentiate iodine and calcium has numerous clinical applications. CT angiography (CTA) of the head and neck is increasingly used to evaluate cerebral aneurysms, arterial stenosis, and other vascular diseases. However, the vasculature near the bony structures, especially at the base of the skull and near the cervical vertebrae, is often difficult to visualize. Segmentation and removal of bony structures based on a single energy CT scan sometimes fails, especially very close to bones or calcified plaque. Subtraction of pre- and post-contrast scans can remove bone, leaving only the iodinated vessels. However, any motion, even swallowing, leads to imperfect subtraction. On the other hand, DECT employs well-registered low and high energy scans to differentiate between iodine and bone, thereby providing bone-removed images that potentially improve the assessment of the vasculature for problems such as aneurysms or vessel lumen narrowing. Because calcified plaque has bone-like spectral properties, it too is removed. The DECT scans may achieve this at lower dose than CTA[49-50]. The same automatic bone- and plaque-removal techniques can be applied to peripheral artery imaging, such as for assessment of stenosis in the femoral arteries since the femur and calcifications no longer obstruct visualization of the lumen. Automated DE-CTA is more reliable than and does not require the time-consuming post-processing of conventional CTA that does not utilize a pre-contrast scan[51-53].

In other applications, the distribution of a specific material may be of interest. Modern DECT scanners have enough volumetric coverage and rotate fast enough to freeze heart motion and obtain high resolution anatomical information as well as spectral information for material specific imaging. An important potential application is the study of myocardial perfusion, which assesses the impact of coronary artery stenoses on myocardial ischemia[54-55]. Administered iodine contrast is blocked by stenoses and is present in lower concentrations in regions of ischemia. DECT is beneficial for CT perfusion studies since it can form iodine-specific images rather than relying on CT numbers alone and since it can correct for beam hardening effects. One of the challenges, however, is that material-specific images can be very noisy compared to normal CT images. Similarly, DECT is also used to diagnose pulmonary embolism by imaging lung perfusion[56]. After iodine contrast is administered, the DECT scan reveals the 3D distribution of iodinated blood. Regions of the lungs devoid or deficient of iodine clearly indicate reduced perfusion in

these regions of the lung. The diagnostic accuracy of detecting pulmonary embolism with DECT has been shown to be higher than that of perfusion scintigraphy, the prevailing technology[57-58].

Imaging of iodine distribution is important to various other clinical applications. Following stent graft placement for aortic aneurysms, it is important to monitor the stent for endoleaks, or unintended blood flow outside the lumen of the graft. Conventional CT imaging requires a non-contrast scan, and post-contrast arterial and venous phase images, but a DECT during the venous phase can obviate the need for the pre-contrast scan. The virtual non-contrast is a reasonable approximation to the true non-contrast study with the additional benefit of perfect image registration and operational efficiency[59-61]. The iodine image may also be useful as a biomarker for angiogenesis and tumor extravasations, which indicate whether a nodule or lesion is likely to be malignant (Fig.8). In lung nodules, small calcifications are suggestive of benign nodules, while abnormal iodine enhancement may indicate malignancy[62]. Iodine images are also used in the detection of hypervascular liver lesions[63] and renal masses[64-65], where a single phase DECT scan may replace multiphase studies by providing both an iodine image and a virtual non-contrast image in which the iodine has been removed.

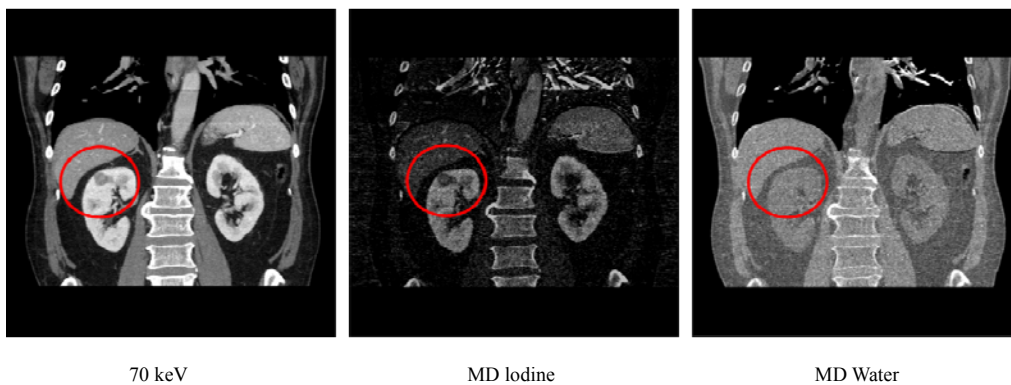70 keV   MD Iodine   MD Water

Fig. 8   DECT is used to classify this mass as an enhancing renal lesion. The water material decomposition image shows the lesion is isointense with the surrounding tissue, which rules out a fatty lesion or hypodense cyst. Further, the iodine image shows enhancement in the lesion (albeit not to the degree that the rest of the kidney enhances, but there is still iodine present), suggesting that the lesion is vascularized. This leads to a diagnosis of renal cell carcinoma[66]. Note that the 70 keV monoenergetic image has much lower noise than the iodine or water material decomposition images since it combines information from both. These images were acquired with a single-phase, contrast-enhanced protocol. Images courtesy of Dr. Amy Hara, Mayo Clinic, Scottsdale, AZ

DECT can also be used for imaging materials other than iodine. For example, atherosclerotic plaque can result in different clinical outcomes depending not only on the narrowing of the lumen, but also on the composition of the plaque. Therefore, DECT has been investigated for its ability to discriminate among fatty, fibrous, or calcified arterial plaque[67]. Another application of DECT is the imaging of lung ventilation with stable (non-radioactive) xenon ($Z = 54$). The inert gas is administered to the patient, and DECT can be used to form xenon-specific images of the lungs to study ventilation[68]. Tendons and ligaments have been shown to be differentiable from soft tissue due to their collagen content, although the results appear to be noisy and may require image post processing[69-71]. Further, DECT is being used to differentiate between different types of renal stones. Uric acid stones can be dissolved via alkalinization of the urine, while large non-uric acid

stones, which usually contain calcium, often must be removed through invasive procedures or external shock wave lithotripsy. Therefore, it is important to differentiate between the two types so that the proper treatment can be prescribed. Because uric acid and the calcium in non-uric acid stones have fairly large difference in Z_{eff} and DEI, they are easy to differentiate with DECT[72-73]. Detection of uric acid is also useful for diagnosing gout, which is a painful condition caused by the buildup of uric acid in the joints[74-75].

Finally, DECT also may have applications in radiation treatment planning. Using the spatial distribution of Z_{eff} and ρ_e obtained from DECT, Bazalova et al demonstrated that Monte Carlo dose calculations could predict the delivered dose in radiation therapy treatment with much higher accuracy than conventional segmentation of single-energy CT images[76]. Furthermore, use of an MV beam has been investigated for use as the high energy scan[77]. In this energy range, attenuation is dominated by Compton scattering, so a kV beam is still needed to provide information about the photoelectric absorption component.

4   Future Directions

Many of the clinical applications in the previous section are still being actively investigated, and DECT technology is continuing to evolve. Methods for more dose efficient dual energy techniques, estimation, and noise reduction are also all active areas of research. DECT is a rich area for research, and we cannot cover all the work here. Rather, in this section, we will touch on two promising technical developments – photon counting and synthetic CT.

4.1   Photon Counting

In addition to the dual energy implementations previously described, another approach that is a very active area of research is energy-resolving photon counting detectors[33,78-81]. These detectors are designed to be extremely fast – fast enough to count each individual photon as it arrives at the detector.   The detector is additionally designed to discern the energy of the photon so that spectral information about the transmitted X-rays can be obtained from a polyenergetic, single kVp exposure. Two key characteristics separate photon counting detectors currently under investigation from the conventional energy integrating detectors used for CT: direct conversion and very fast circuitry. Rather than relying on indirect conversion of X-rays first to light and then to an electrical signal, these photon counting detectors utilize direct conversion materials such as semiconductors Si, CdZn, or CdZnTe or xenon gas that can directly generate a signal by producing electrons when an X-ray is absorbed. Unlike the relatively long light pulse produced by most CT scintillators (relative to the arrival rate of photons), direct conversion materials produce a very short signal that is shaped and counted by very fast circuitry, operating on a clock cycle on the order of several hundred MHz.

Photon counting detectors have been used in nuclear medicine for a number of years, where measuring the arrival time and energy of photons is essential but the flux rates are much lower than in CT[82]. In unattenuated regions of the beam, CT count rates can easily exceed 100 million counts per second per mm^2 at 1 m distance. If the detector's count rate cannot keep up, it will experience count rate losses as it fails to count all photons and spectral distortion as the photon signals temporally overlap (also called pileup)[81]. Nonetheless, as photon counting technology has progressed, it is actively being investigated for use in CT. If these detectors could be fast enough and have a good spectral response, a number of key advantages can be exploited. Ideal photon

counting detectors are known to be more dose efficient than energy integrating detectors because of the additional energy information made available[83-84], which is usually recorded as the number of counts within different energy windows or bins. At least two energy bins are necessary so that a low energy bin and a high energy bin can effectively provide dual energy information, but more bins provide more spectral information and better material decomposition estimation.

Most exciting though, is the idea that with multiple energy bins, there can be multiple basis functions. This requires the use of K-edge contrast agents like iodine, gadolinium, or gold. Iodine is ubiquitous in clinical CT, gadolinium is commonly used in MR, and gold is being investigated for targeted delivery in nanoparticles[85]. For example, to uniquely form a basis image from iodine, there should be a bin above and below its K-edge at 33.2 keV. Multiple contrast agents could be used simultaneously if there are enough bins. This has been recently demonstrated preclinically and has the potential to image multiple pathways or processes simultaneously[85-86].

4.2 Synthetic CT

In our own work with dual energy CT, we have recently introduced a novel application known as synthetic CT[87-88]. With synthetic CT, users can retrospectively synthesize clinical images from arbitrary low dose CT protocols, including changes to tube voltage, current, and filtration. The synthesized images appear as if they were acquired with the alternate protocol and accurately reflect the contrast and noise of this protocol. With such a tool, it is possible to study the effect of protocol selection on image quality and dose distribution, enabling CT users to perform task-dependent protocol optimization using previously collected clinically relevant data. In particular, as technology advances and we strive to reduce dose according to the ALARA (As Low As Reasonably Achievable) principle, we need to be confident that lower dose protocols can still yield diagnostic quality images.

As can be seen in Fig. 9, images for a wide range of parameters can be synthesized. Yet, the only data that needs to be acquired is a dual energy scan (in this case, at 80 and 140 kVp). Most notably, the kVp, mAs, and filtration can be freely adjusted. In Fig. 9, an image is synthesized for a 120 kVp, 250 mAs protocol with mA modulation and has the same contrast and noise properties as if the phantom were actually scanned with this protocol. Furthermore, the effect of a virtual object can be simulated by loading a physical description of the object so that the effect of its attenuation can be included in the detected signal and noise calculations. The dose distribution can be determined due to the information provided by DECT, as previously mentioned. Although not shown here, synthetic CT can also synthesize the material decomposition images from dual energy protocols other than what was acquired, such as different kVp pairs or mAs allocation[88].

Synthetic CT is made possible by a dual energy scan, which provides a material decomposition in projection space. As previously discussed, this material decomposition completely characterizes the X-ray attenuation along all line integrals at all energies. Therefore, the transmission of any other spectrum along each line integral can be determined and used to predict the mean detected signal. Moreover, the target noise level at the detector can be predicted based on the transmitted number of photons. This is compared to the inherent noise level that is present due to uncertainty in the material decomposition since the original dual energy scan itself has noise. Noise is then added to bring the inherent noise up to the target noise level, which is necessary to accurately synthesize the increased noise in low dose protocols. The synthesized sinograms are then reconstructed.

To verify the accuracy of synthetic CT, we have compared synthesized images at a number of

protocols to actual images with a phantom (verification cannot be carried out on a patient!) and found excellent agreement. We are now in the beginning stages of developing synthetic CT into a tool that radiologists can use to understand how CT protocol selection affects tradeoffs involved in dose and image quality.
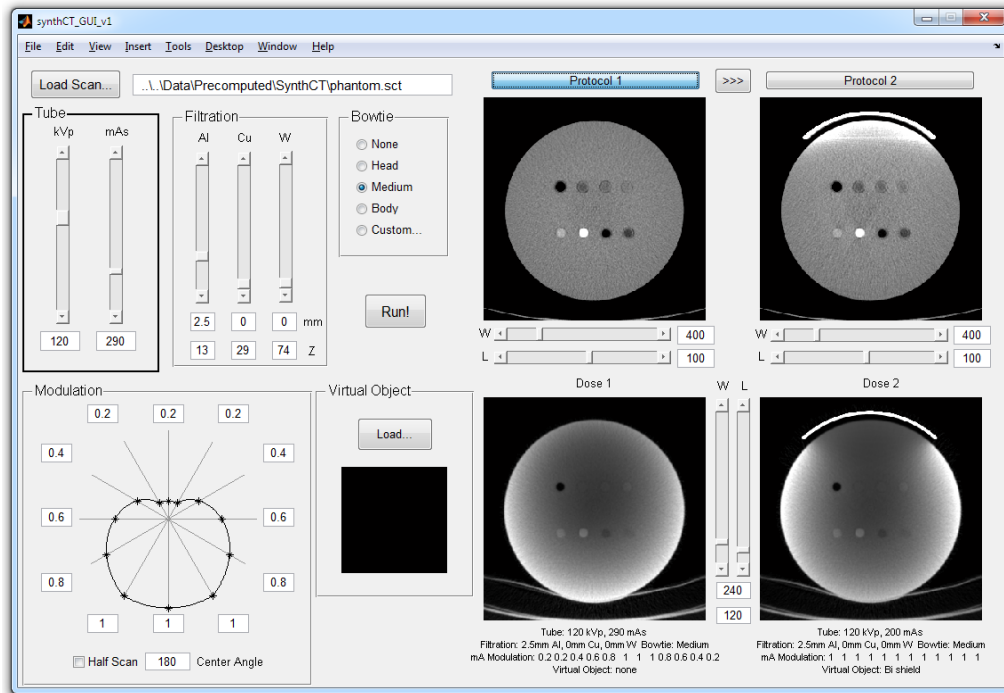

Fig. 9   Synthetic CT GUI with protocol 1 simulating mA modulation and protocol 2 simulating a virtual breast shield[89]. The top left sliders allow the user to adjust kVp and mAs. To the right, the user selects filtration materials and thicknesses and bowtie. In the bottom left, we see the mA modulation profile for the active protocol – protocol 1 – which has no virtual objects, so the virtual object thumbnail is blank. The top row of images are the synthesized images, the bottom row are the dose profiles, the left column is protocol 1, and the right column is protocol 2, providing a side-by-side comparison

5   Conclusions

For materials normally found in vivo and within the diagnostic X-ray spectrum, the fundamental X-ray physics suggests that there are only two primary attenuation mechanisms, so measurements at two energies allow for estimation of object-specific properties related to its composition. This material specific imaging is quantitative and leads to increased diagnostic confidence based on the distribution of a material of interest, such as iodine contrast. Furthermore, a number of surprising and novel applications have been developed, such as the increased accuracy of radiation therapy treatment planning and synthetic CT. Clearly, dual energy CT is an exciting area of growth and research. It has many benefits in clinical applications and will continue to see increased use as technology continues to advance and as more CT systems deploy this technology.

References

[1] Hounsfield G. Computerized transverse axial scanning (tomography): Part 1. description of system[J]. British Journal of Radiology, 1973, 46(552): 1016.

[2] Alvarez R, Macovski A. Energy-selective reconstructions in X-ray computerised tomography[J]. Physics in Medicine and Biology, 1976, 21: 733-744.

[3] Rutherford R, Pullan B, Isherwood I. Measurement of effective atomic number and electron density using an EMI scanner[J]. Neuroradiology, 1976, 11(1): 15-21.

[4] Di Chiro G, Brooks R, Kessler R, et al. Tissue signatures with dual-energy computed tomography[J]. Radiology, 1979, 131(2): 521.

[5] Millner M, McDavid W, Waggener R, et al. Extraction of information from CT scans at different energies[J]. Medical Physics, 1979, 6: 70.

[6] Kelcz F, Joseph P, Hilal S. Noise considerations in dual energy CT scanning[J]. Medical Physics, 1979, 6(5): 418-425.

[7] Kalender W, Perman W, Vetter J, et al. Evaluation of a prototype dual-energy computed tomographic apparatus. I. Phantom studies[J]. Medical Physics, 1986, 13: 334.

[8] Rutt B, Fenster A. Split-filter computed tomography: A simple technique for dual energy scanning[J]. Journal of Computer Assisted Tomography, 1980, 4(4): 501.

[9] Ritchings R, Pullan B. A technique for simultaneous dual energy scanning[J]. Journal of Computer Assisted Tomography, 1979, 3(6): 842.

[10] Marshall W, Alvarez R, Macovski A. Initial results with prereconstruction dual-energy computed tomography (PREDECT)[J]. Radiology, 1981, 140(2): 421-430.

[11] Marshall W, Hall E, Doost-Hoseini, et al. An implementation of dual energy CT scanning[J]. Journal of Computer Assisted Tomography, 1984, 8(4): 745.

[12] Lehmann L, Alvarez R, Macovski, et al. Generalized image combinations in dual KVP digital radiography[J]. Medical Physics, 1981, 8: 659-667.

[13] Genant H, Boyd D. Quantitative bone mineral analysis using dual energy computed tomography[J]. Investigative Radiology, 1977, 12(6): 545.

[14] Adams J, Chen S, Adams P, et al. Measurement of trabecular bone mineral by dual energy computed tomography[J]. Journal of Computer Assisted Tomography, 1982, 6(3): 601.

[15] Vetter J, Perman W, Kalender W, et al. Evaluation of a prototype dual-energy computed tomographic apparatus. II. Determination of vertebral bone mineral content[J]. Medical Physics, 1986, 13: 340.

[16] Kalender W, Klotz E, Suess C. Vertebral bone mineral analysis: An integrated approach with CT[J]. Radiology, 1987, 164(2): 419-423.

[17] Goldberg H, Cann C, Moss A, et al. Noninvasive quantitation of liver iron in dogs with hemochromatosis using dual-energy CT scanning[J]. Nvestigative Radiology, 1982, 17(4): 375.

[18] Cann C, Gamsu G, Birnberg F, et al. Quantification of calcium in solitary pulmonary nodules using single-and dual-energy CT[J]. Radiology, 1982: 145(2): 493.

[19] Macovski A. Medical imaging systems[J]. Prentice-Hall, 1983.

[20] Primak A, Giraldo J, Liu X, et al. Improved dual-energy material discrimination for dual-source CT by means of additional spectral filtration[J]. Medical Physics, 2009, 36(4): 1359-1369.

[21] Primak A, Giraldo J, Eusemann C, et al. Dual-source dual-energy CT with additional tin filtration: Dose and

image quality evaluation in phantoms and in vivo[J]. American Journal of Roentgenology, 2010, 195(5): 1164.

[22] Petersilka M, Stierstorfer K, Bruder H, et al. Strategies for scatter correction in dual source CT[J]. Medical Physics, 2010, 37: 5971.

[23] Xu D, Langan D, Wu X, et al. Dual energy CT via fast kVp switching spectrum estimation[C]//Proceedings of SPIE, 2009, 7258, 72583T.

[24] Goodsitt M, Christodoulou E, Larson S. Accuracies of the synthesized monochromatic CT numbers and effective atomic numbers obtained with a rapid kVp switching dual energy CT scanner[J]. Medical Physics, 2011, 38: 2222-2232.

[25] Yu L, Primak A, Liu X, et al. Image quality optimization and evaluation of linearly mixed images in dual-source, dual-energy CT[J]. Medical Physics, 2009, 36: 1019.

[26] Schenzle J, Sommer W, Neumaier K, et al. Dual energy CT of the chest: How about the dose?[J]. Investigative Radiology, 2010, 45(6): 347.

[27] Barnes G, Sones R, Tesic M, et al. Detector for dual-energy digital radiography[J]. Radiology, 1985, 156(2): 537-540.

[28] Gauntt D, Barnes G. X-ray tube potential, filtration, and detector considerations in dual-energy chest radiography[J]. Medical Physics, 1994, 21: 203.

[29] Alvarez R, Seibert J, Thompson S. Comparison of dual energy detector system performance[J]. Medical Physics, 2004, 31: 556.

[30] Holmes III D, Fletcher J, Apel A, et al. Evaluation of non-linear blending in dual-energy computed tomography[J]. European Journal of Radiology, 2008, 68(3): 409-413.

[31] Krauss B, Schmidt B, Flohr T. Dual source CT, dual energy CT in clinical practice[M]. 2011: 11-20.

[32] Fessler J, Elbakri I, Sukovic P, et al. Maximum-likelihood dual-energy tomographic image reconstruction[C]//Proceedings of SPIE: Medical Imaging 2002: Image Processing, 2002, 4684: 38-49.

[33] Schlomka J, Roessl E, Dorscheid R, et al. Experimental feasibility of multi-energy photon-counting K-edge imaging in pre-clinical computed tomography[J]. Physics in Medicine and Biology, 2008, 53: 4031-4047.

[34] Roessl E, Herrmann C. Cramer–Rao lower bound of basis image noise in multiple-energy X-ray imaging[J]. Physics in Medicine and Biology, 2009, 54: 1307-1318.

[35] Alvarez R. Estimator for photon counting energy selective X-ray imaging with multibin pulse height analysis[J]. Medical Physics, 2011, 38: 2324.

[36] Cardinal H, Fenster A. An accurate method for direct dual-energy calibration and decomposition[J]. Medical Physics, 1990, 17: 327.

[37] Maaß C, Meyer E, Kachelrieß M. Exact dual energy material decomposition from inconsistent rays (MDIR)[J]. Medical Physics, 2011, 38: 691.

[38] Brody W, Cassel D, Sommer F, et al. Dual-energy projection radiography: Initial clinical experience[J]. American Journal of Roentgenology, 1981, 137(2): 201.

[39] Mazess R, Barden H, Bisek J, et al. Dual-energy X-ray absorptiometry for total-body and regional bone-mineral and soft-tissue composition[J]. American Journal of Clinical Nutrition, 1990, 51(6): 1106.

[40] Adams J. Single and dual energy X-ray absorptiometry[J]. European Radiology, 1997, 7(2): 20.

[41] Fainberg A. Explosives detection for aviation security[J]. Science, 1992, 255(5051): 1531.

[42] Singh S, Singh M. Explosives detection systems (EDS) for aviation security[J]. Signal Processing, 2003, 83(1): 31-55.

[43] Ying Z, Naidu R, Crawford C. Dual energy computed tomography for explosive detection[J]. Journal of X-ray Science and Technology, 2006, 14(4): 235-256.

[44] Robert-Coutant C, Moulin V, Sauze R, et al. Estimation of the matrix attenuation in heterogeneous radioactive waste drums using dual-energy computed tomography[J]. Nuclear Instruments and Methods in Physics Research Section A, 1999, 422(1): 949-956.

［45］ Gehrke S, Wirth K. Application of conventional- and dual-energy X-ray tomography in process engineering[J]. IEEE Sensors Journal, 2005, 5(2): 183-187.

［46］ Van Geet M, Swennen R, Wevers M. Quantitative analysis of reservoir rocks by microfocus X-ray computerised tomography[J]. Sedimentary Geology, 2000, 132(1): 25-36.

［47］ Rogasik H, Crawford J, Wendroth O, et al. Discrimination of soil phases by dual energy X-ray tomography[J]. Soil Science Society of America Journal, 1999, 63(4): 741-751.

［48］ Johnson T, Fink C, Schonberg S, et al. Dual energy CT in clinical practice[M]. Springer-Verlag Berlin Heidelberg, 2011.

［49］ Deng K, Liu C, Ma R, et al. Clinical evaluation of dual-energy bone removal in CT angiography of the head and neck: Comparison with conventional bone-subtraction CT angiography[J]. Clinical Radiology, 2009, 64(5): 534-541.

［50］ Uotani K, Watanabe Y, Higashi M, et al. Dual-energy CT head bone and hard plaque removal for quantification of calcified carotid stenosis: Utility and comparison with digital subtraction angiography[J]. European Radiology, 2009, 19(8): 2060-2065.

［51］ Meyer B, Werncke T, Hopfenmuller, et al. Dual energy CT of peripheral arteries: Effect of automatic bone and plaque removal on image quality and grading of stenoses[J]. European Journal of Radiology, 2008, 68(3): 414-422.

［52］ Brockmann C, Jochum S, Sadick M, et al. Dual-energy CT angiography in peripheral arterial occlusive disease[J]. Cardiovascular and Interventional Radiology, 2009, 32(4): 630-637.

［53］ Tran D, Straka M, Roos J, et al. Dual-energy CT discrimination of iodine and calcium: Experimental results and implications for lower extremity CT angiography[J]. Academic Radiology, 2009, 16(2): 160-171.

［54］ Ruzsics B, Lee H, Zwerner P, et al. Dual-energy CT of the heart for diagnosing coronary artery stenosis and myocardial ischemia-initial experience[J]. European Radiology, 2008, 18(11): 2414-2424.

［55］ Ko S, Choi J, Song M, et al. Myocardial perfusion imaging using adenosine-induced stress dual-energy computed tomography of the heart: Comparison with cardiac magnetic resonance imaging and conventional coronary angiography[J]. European Radiology, 2010: 1-10.

［56］ Chae E, Seo J, Jang Y, et al. Dual-energy CT for assessment of the severity of acute pulmonary embolism: Pulmonary perfusion defect score compared with CT angiographic obstruction score and right ventricular/ left ventricular diameter ratio[J]. American Journal of Roentgenology, 2010, 194(3): 604.

［57］ Zhang L, Chai X, Wu S, et al. Detection of pulmonary embolism by dual energy CT: Correlation with perfusion scintigraphy and histopathological findings in rabbits[J]. European Radiology, 2009, 19(12): 2844-2854.

［58］ Thieme S, Becker C, Hacker M, et al. Dual energy CT for the assessment of lung perfusion–correlation to scintigraphy[J]. European Journal of Radiology, 2008, 68(3): 369-374.

［59］ Stolzmann P, Frauenfelder T, Pfammatter T, et al. Endoleaks after endovascular abdominal aortic aneurysm repair: Detection with dual-energy dual-source CT[J]. Radiology, 2008, 249(2): 682.

［60］ Chandarana H, Godoy M, Vlahos I, et al. Abdominal aorta: Evaluation with dual-source dual-energy multidetector CT after endovascular repair of aneurysms – initial observations[J]. Radiology, 2008, 249(2): 692.

［61］ Sommer W, Graser A, Becker C, et al. Image quality of virtual noncontrast images derived from dual-energy CT angiography after endovascular aneurysm repair[J]. Journal of Vascular and Interventional Radiology, 2010, 21(3): 315-321.

［62］ Chae E, Song J, Seo J, et al. Clinical utility of dual-energy CT in the evaluation of solitary pulmonary nodules: Initial experience[J]. Radiology, 2008, 249(2): 671.

［63］ Kim K, Lee J, Kim S, et al. Image fusion in dual energy computed tomography for detection of hypervascular liver hepatocellular carcinoma: Phantom and preliminary studies[J]. Investigative Radiology, 2010, 45(3): 149.

［64］ Graser A, Johnson T, Hecht E, et al. Dual-energy CT in patients suspected of having renal masses: Can virtual nonenhanced images replace true nonenhanced images[J]. Radiology, 2009, 252(2): 433.

［65］ Graser A, Becker C, Staehler M, et al. Single-phase dual-energy CT allows for characterization of renal masses as benign or malignant[J]. Investigative Radiology, 2010, 45(7): 399.

［66］ Silva A, Morse B, Hara A, et al. Dual-energy (spectral) CT: Applications in abdominal imaging[J]. RadioGraphics, 2011, 31(4): 1031-1046.

［67］ Barreto M, Schoenhagen P, Nair A, et al. Potential of dual-energy computed tomography to characterize atherosclerotic plaque: Ex vivo assessment of human coronary arteries in comparison to histology[J]. Journal of Cardiovascular Computed Tomography, 2008, 2(4): 234-242.

［68］ Chae E, Seo J, Goo H, et al. Xenon ventilation CT with a dual-energy technique of dual-source CT: Initial experience[J]. Radiology, 2008, 248(2): 615.

［69］ Johnson T, Krauß B, Sedlmair M, et al. Material differentiation by dual energy CT: Initial experience[J]. European Radiology, 2007, 17(6): 1510-1517.

［70］ Sun C, Miao F, Wang X, et al. An initial qualitative study of dual-energy CT in the knee ligaments[J]. Surgical and Radiologic Anatomy, 2008, 30(5): 443-447.

［71］ Deng K, Sun C, Liu C, et al. Initial experience with visualizing hand and foot tendons by dual-energy computed tomography[J]. Clinical Imaging, 2009, 33(5): 384-389.

［72］ Primak A, Fletcher J, Vrtiska T, et al. Noninvasive differentiation of uric acid versus non-uric acid kidney stones using dual-energy CT[J]. Academic Radiology, 2007, 14(12): 1441-1447.

［73］ Graser A, Johnson T, Bader M, et al. Dual energy CT characterization of urinary calculi: Initial in vitro and clinical experience[J]. Investigative Radiology, 2008, 43(2): 112.

［74］ Johnson T, Weckbach S, Kellner H, et al. Clinical image: Dual-energy computed tomographic molecular imaging of gout[J]. Arthritis & Rheumatism, 2007, 56(8): 2809-2809.

［75］ Choi H, Al-Arfaj A, Eftekhari A, et al. Dual energy computed tomography in tophaceous gout[J]. Annals of the Rheumatic Diseases, 2009, 68(10): 1609.

［76］ Bazalova M, Carrier J, Beaulieu L, et al. Dual-energy CT-based material extraction for tissue segmentation in Monte Carlo dose calculations[J]. Physics in Medicine and Biology, 2008, 53: 2439-2456.

［77］ Yang M, Virshup G, Clayton J, et al. Does kV–MV dual-energy computed tomography have an advantage in determining proton stopping power ratios in patients[J]. Physics in Medicine and Biology, 2011, 56(14), 4499-4515.

［78］ Shikhaliev P. Energy-resolved computed tomography: First experimental results[J]. Physics in Medicine and Biology, 2008, 53: 5595.

［79］ Barber W, Nygard E, Wessel J, et al. Large area photon counting X-ray imaging arrays for clinical dual-energy applications[C]//Nuclear Science Symposium Conference Record (NSS/MIC): 2009, IEEE, 3029-3031, IEEE (2009).

［80］ Barber W, Nygard E, Iwanczyk J, et al. Characterization of a novel photon counting detector for clinical CT: Count rate, energy resolution, and noise performance[C]//Proceedings of SPIE, 7258, 725824 (2009).

［81］ Wang A, Harrison D, Lobastov V, et al. Pulse pileup statistics for energy discriminating photon counting X-ray detectors[J]. Medical Physics, 2011, 38: 4265.

［82］ Knoll G. Radiation detection and measurement[J]. John Wiley and Sons, New York: 1979.

［83］ Tapiovaara M, Wagner R. SNR and DQE analysis of broad spectrum X-ray imaging[J]. Physics in Medicine and Biology, 1985, 30: 519.

［84］ Wang A, Pelc N. Sufficient statistics as a generalization of binning in spectral X-ray imaging[J]. Medical Imaging, IEEE Transactions on 2011, 30(1): 84-93.

［85］ Cormode D, Roessl E, Thran A, et al. Atherosclerotic plaque composition: Analysis with multicolor CT and targeted gold nanoparticles[J]. Radiology, 2010, 256(3): 774.

［86］ Wang X, Meier D, Taguchi K, et al. Material separation in X-ray CT with energy resolved photon-counting

detectors[C]//Proceedings of SPIE, 2011, 7961: 79611V.

［87］ Wang A, Pelc N. Synthetic CT: Simulating arbitrary low dose single and dual energy protocols[C]// Proceedings of SPIE, 2011, 7961: 79611R.

［88］ Wang A, Pelc N. Synthetic CT: Simulating low dose single and dual energy protocols from a dual energy scan[J]. Medical Physics, 2011, 38(10): 5551.

［89］ Vollmar S, Kalender W. Reduction of dose to the female breast in thoracic CT: A comparison of standard-protocol, bismuth-shielded, partial and tube-current-modulated CT examinations[J]. European Radiology, 2008, 18(8): 1674-1682.

双能 **CT** 的基本原理、应用和未来展望

Adam S. WANG[a,b][⊠], Scott S. HSIEH[a,b], Norbert J. PELC[a,b,c]

Departments of a).Electrical Engineering, b).Radiology, and
c).Bioengineering; Stanford University, Stanford, CA 94305

摘要：断层影像（CT）的图像对比度与扫描所用的 X 光源能谱分布有很大关系。传统 CT 使用具有能谱分布的一个光源进行成像，有时会出现信息模糊致使两种不同材料在 CT 图像上完全相同。双能 CT 使用两个不同分布的能谱对物体进行成像，能够消除单能谱情况下的信息模糊。虽然双能 CT 的基本概念由来已久，但最近商业系统的出现使双能 CT 迅速成为一个热点。我们首先概述了双能 CT 的基本物理原理和双能信号处理方法，包括促使双能 CT 进入现代医学成像的关键技术。其次，双能 CT 的应用已非常广泛，本文从其在临床应用角度进行了详细介绍使读者有所了解。最后，我们简要探讨了当前的两个技术发展领域：光子技术探测器和技术合成 CT。

关键词：双能；材料分解；双源；光子计算；合成 CT

Biography: Adam Wang[⊠] is a PhD candidate in Electrical Engineering at Stanford University, where he is studying under the supervision of Prof. Norbert Pelc. Mr. Wang's research interests include medical image reconstruction, signal processing, and information theory. He received his BSEE in 2006 from the University of Texas at Austin and his MSEE in 2008 from Stanford University. E-mail: adamwang@stanford.edu.